High-speed rotary microvalves in water using hydrodynamic force due to induced-charge electrophoresis

Hideyuki Sugioka*

Frontier Research Center, Canon Inc., 30-2 Shimomaruko 3-chome, Ohta-ku, Tokyo, Japan

The development of a high-speed microactuator in water is difficult because of electrostatic problems and hydrodynamic resistance. To overcome these problems, we consider using induced-charge electrophoresis (ICEP) to move actuators. We propose rotary microvalves in water using hydrodynamic force due to ICEP and numerically examine the performance of valves. By the multiphysics coupled simulation technique between fluidics and electrostatics based on the boundary element method along with the thin-double-layer approximation, we find rotary valves using ICEP function effectively at high frequency. In the calculations, the electric and flow field problems in a bounded domain are solved, and the proper boundary conditions are discussed. By employing similar actuators using ICEP, we can dramatically improve the performance of promising microfluidic systems such as lab-on-a-chip.

PACS number(s): 47.57.−s, 85.90.+h, 82.45.Hk, 83.50.Lh

I. INTRODUCTION

A hydrodynamic resistance due to viscosity increases rapidly in a microchannel as the width of the channel decreases. Thus, the development of a high-speed microactuator in water is challenging, although the development of a high-speed microactuator in air by using electrostatic force is common in the field of microelectromechanical systems (MEMS). In particular, it is very challenging to develop microvalves that function in water at high speeds similar to those of an electrostatic valve in air because valves are indispensable for controlling flows in microchannels with mixers and pumps in promising biomedical applications such as lab-on-a-chip [1], and they are intrinsically movable devices. Note that large pressure-driven valves are still used reluctantly for the design of lab-on-a-chip.

Recently, several researchers [2,3] have observed motion in water using induced-charge electrophoresis (ICEP). ICEP is different from classical electrophoresis because it results from the interaction between the electric field and ions in the electric double layer formed by the polarizing effect of the electric field itself [2,4–14]. In particular, Gangwal *et al.* [2] observed the motion of a half-coated metal sphere using ICEP and suggested its application to various devices. Moreover, the rotation of micrometallic rods has been studied theoretically [15] and experimentally [3]. However, no attempt has been made to analyze microvalves that use ICEP. To overcome the problems faced by actuators in water, we consider using ICEP to move valves and then stop and release the flow of the channel. In particular, rotary-ICEP valves have the potential to avoid viscosity problems since they are expected to move smoothly by using the slip velocity on the surface. Thus, in this paper, we focus on the development of a rotary-ICEP valve in water using hydrodynamic force due to ICEP and elucidate its design concept. In particular, we consider a rotary-ICEP valve that can be opened by the pressure gradient without an electric field and

can be closed by an electric field perpendicular to the channel wall to avoid complex geometries for electrodes. Further, for the valve problem, the metal cylinder is very close to the wall in order to sufficiently stop the flow. Thus, in the calculations, the electric and flow field problems in the bounded domain are solved, and the proper boundary conditions are discussed.

This paper is presented in five sections. In Sec. II, we describe the theory for a geometry model, a flow model, a slip velocity model for bounded and unbounded domains, an electrorotational torque model for bounded and unbounded domains, and a simple model for a multi rotary-ICEP valve. Based on these models, the results for the boundary effects on ICEP, the basic design of Nth rotary-ICEP valve, the performance of a single rotary-ICEP valve, and the performance of a twin rotary-ICEP valve are presented in Sec. III. Following a discussion in Sec. IV, our conclusions are summarized in Sec. V.

II. THEORY

A. Geometry model

Figure 1 shows the schematic view of the rotary-ICEP valve considered in this study. In Fig. 1, we place an elliptical metal cylinder of length $2b$ and width $2c$ in a rectangular channel of length $L = 2.25w$ and width $w = 100$ μm. The center of the cylinder of a single rotary valve is anchored near the center of the channel but is free for rotation. Similarly, we can consider other valves using multielliptical cylinders, as shown in Figs. 2 and 16. Note that these rotary-ICEP valves have an intrinsically two-dimensional (2D) structure. Moreover, we can probably neglect the friction between the substrate and the elliptical cylinder by considering a hydrodynamic repulsion that considerably reduces the friction between a spindle of the valve and a bearing.

B. Flow model

We consider a 2D quasistatic Stokes flow without Brownian motion, i.e., we consider the limit in which the Reynolds
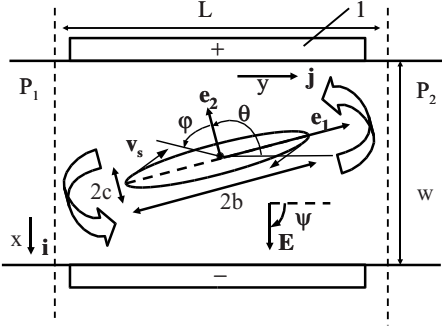
*sugioka.hideyuki@canon.co.jp

FIG. 1. Schematic view of rotary-ICEP valve. 1: pair of electrodes. Here, $\psi=0$ and $\pi/2$ rad for parallel and vertical electric fields, respectively; length $L=2.25w$ and width $w=100$ μm. The ellipse has two semiaxes (b,c) with unit vectors (e_1,e_2) that define the orientation of each semiaxis.

number Re tends to zero and the Peclet number is infinite. We assume the posts of the elliptical cylinder to be polarizable in an electrolytic solution under a dc or ac electric field. The motion of the surrounding fluid must satisfy Stokes equations modified by the inclusion of an electrical stress. However, by using matched asymptotic expansion [16], we can reduce them to the classical Stokes equations as follows:

$$\mu\nabla^2\boldsymbol{v} - \nabla p = 0, \quad \boldsymbol{\nabla}\cdot\boldsymbol{v} = 0, \tag{1}$$

$$\text{on } S_p^+ : \boldsymbol{v} = \boldsymbol{U} + \boldsymbol{\Omega}\times\boldsymbol{x} + \boldsymbol{v}_s, \tag{2}$$

$$\int_{S_p^+}\boldsymbol{f}dl + \boldsymbol{F}_t^{\text{ext}} = 0, \quad \int_{S_p^+}\boldsymbol{x}\times\boldsymbol{f}dl + \boldsymbol{T}_t^{\text{ext}} = 0, \tag{3}$$

where S_p^+ denotes the surface defined as the outer edge of the double layer; $\boldsymbol{U}$ is the translational velocity; $\boldsymbol{\Omega}$ is the rotational angular velocity; $\boldsymbol{f}$ is the traction vector; $\boldsymbol{F}_t^{\text{ext}}$ and $\boldsymbol{T}_t^{\text{ext}}$ are the total external force and torque, respectively, on the elliptical metal cylinder; $\boldsymbol{x}$ is the surface position of metals parametrized by φ, $\mu(\sim1$ mPa s$)$ is the viscosity; $\boldsymbol{v}$ is the velocity; $\boldsymbol{v}_s$ is the slip velocity; and p is the pressure. Note that we use the boundary condition that the velocity on the wall of the channel is zero and that the pressures of the inlet and outlet are P_1 and P_2, respectively. (Here, $\Delta P=P_2-P_1$.) We calculate the flow fields of the ICEP valve using the boundary element method based on Eqs. (1)–(3). In particular, to obtain a precise flow field near the wall and the metal surfaces, we use analytical integration to obtain the matrix elements of the boundary element method. Moreover, to
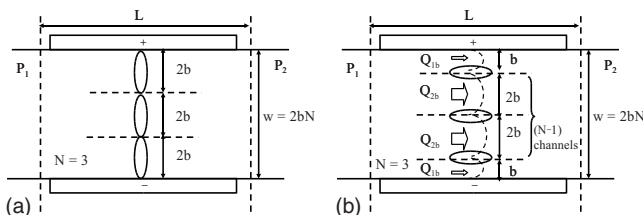

FIG. 2. Schematic view of multi-rotary-ICEP valve $(N=3)$.

evaluate the valve performance we define U_p as the average flow velocity at the inlet.

C. Slip velocity model for a bounded domain

The basic phenomena of ICEP can be understood by considering initial potential state and final potential state when we apply an external field [5,6]. Immediately after an external field $\boldsymbol{E}=E_0\boldsymbol{i}$ is applied to a metal particle, an electric field is set up, so that field lines intersect conducting surfaces at right angles because a metal works as a conductive material. Although this represents the steady-state vacuum field configuration, mobile ions in electrolytic solutions move in response to applied fields. A current $\boldsymbol{J}=\sigma\boldsymbol{E}$ drives positive ions into a charge cloud on one side of the conductor, and negative ions to the other, inducing an equal and opposite surface charge on the conducting surface. A dipolar charge cloud grows as long as a normal field injects ions into the induced double layer, and steady state is achieved when no field lines penetrate the double layer if the induced charge is so small that the surface conduction is negligible. Thus, a zeta potential ζ around a metal is generally defined as follows:

$$\zeta = \phi_i - \phi_f, \tag{4}$$

where ϕ_i is the electric potential of the particle that is equal to the electric potential without the double layer or the initial potential defined in this paper, and ϕ_f is the electric potential just outside the double layer or the final potential defined in this paper, i.e., the zeta potential is the difference between the potential in the metal and the potential just outside the double layer. To model an ICEP-valve problem under a bounded condition, we solve the electric potential at every time step before calculating a flow field by the boundary element method based on the following Laplace's equation:

$$\nabla^2\phi = 0. \tag{5}$$

On the one hand, we use the Dirichlet boundary condition for the upper and lower walls (electrodes), i.e., $\phi=+0.5V_0$ at $x=0$ and $\phi=-0.5V_0$ at $x=w$, where V_0 is an applied voltage across the channel. On the other hand, we use the Neumann boundary condition for the left and right walls, i.e., $\boldsymbol{n}\cdot\nabla\phi=0$ at $y=0$ and L, where $\boldsymbol{n}$ is the surface normal unit vector. In addition to those boundary conditions, to obtain a final potential, we also use the Neumann boundary condition (i.e., $\boldsymbol{n}\cdot\nabla\phi=0$) on the metal surface. Further, to obtain an initial potential, we use the condition that j metal particles have an unknown surface potential $\phi_i^{(j)}$ and require the electrical neutral condition that $\oint_{(j)}(\boldsymbol{n}\cdot\nabla\phi)ds=0$. It should be noted that we are assuming that the ellipsoid is a "floating conductor," i.e., the total charge does not change with time. The ellipsoid does change its potential ϕ_i with time, although it does not change its charge.

Under a wide range of conditions, the local slip velocity is given by the Helmholtz-Smoluchowski formula

$$\boldsymbol{v}_s = -\frac{\varepsilon\zeta}{\mu}\boldsymbol{E}_s, \tag{6}$$

where $\boldsymbol{v}_s$ is the slip velocity, and S_p^+ is the surface defined as the outer edge of the double layer, and $\boldsymbol{E}_s$ is the tangential

component of the electric field. Thus, we can numerically calculate a flow field and an angular velocity of an elliptical cylinder for a bounded domain ($\Omega^{\text{ICEP,bounded}}$).

D. Slip velocity model for an unbounded domain

By using an analytical solution of E_s for an unbounded domain in Appendix A, we can obtain a formulation of a slip velocity and a zeta potential as follows:

$$v_s^{\text{unbounded}} = \tfrac{1}{2}U_c(\alpha+1)^2 q_0^{-1}\sin 2(\psi+\varphi+\theta)t, \quad (7)$$

$$\zeta^{\text{unbounded}} = c(\alpha+1)E_0\cos(\psi+\varphi+\theta), \quad (8)$$

where $q_0 = \sqrt{\alpha^2\cos^2\varphi+\sin^2\varphi}$, $U_c(=\varepsilon cE_0^2/\mu)$ is the representative velocity, $\alpha=b/c$, $x=-b\sin\varphi e_1+c\cos\varphi e_2$, $t=-q_0^{-1}(\alpha\cos\varphi e_1+\sin\varphi e_2)$ is the tangential unit vector of the position, electric field $E=\cos\psi j+\sin\psi i$, $e_2=\cos\theta j-\sin\theta i$, $e_1=\sin\theta j+\cos\theta i$, where i and j are orthogonal unit vectors of the Cartesian coordinate system, $E_0=|E|$, $\mu(\sim 1\ \text{mPa s})$ is the viscosity, $\varepsilon(\sim 80\varepsilon_0)$ is the dielectric permittivity of the solvent (typically water), and ε_0 is the vacuum permittivity. Further, from Eqs. (1)–(3) and based on the three-dimensional (3D) formulation of [16], we find that the 2D angular velocity of the elliptical cylinder in unbounded domain is

$$\mathbf{\Omega}^{\text{ICEP}} = -\frac{1}{\pi bc(b^2+c^2)}\int_{S_p^+}(\mathbf{n}\cdot\mathbf{x})(\mathbf{x}\times\mathbf{v}_s)dl. \quad (9)$$

Thus, by using Eqs. (7) and (9), we find that the 2D angular velocity of the elliptical cylinder in an unbounded domain is

$$\mathbf{\Omega}^{\text{ICEP,unbounded}} = \frac{\varepsilon E_0^2}{\mu}\frac{\alpha^2-1}{\alpha^2+1}\sin 2(\theta+\psi)e_3. \quad (10)$$

Note that we will prove Eq. (10) in Appendix B.

Furthermore, a slip velocity v_s can be calculated by the electric field calculations using Eqs. (4)–(6) for a bounded domain. Therefore, we can also obtain an angular velocity $\mathbf{\Omega}^{\text{method-A}}$ that is predicted by Eqs. (4)–(6) and (9), i.e., by using the slip velocity obtained by the bounded electric field calculation and the analytical prediction for angular velocity using an integral form of Eq. (9). Note that $\mathbf{\Omega}^{\text{method-A}}$ is useful for separating a boundary effect due to the electric field boundary conditions from that due to the flow field boundary conditions. Similarly, we can obtain an angular velocity ($\Omega^{\text{method-B}}$) predicted by Eqs. (1)–(3) and (7), i.e., by using the analytical slip velocity of Eq. (7) and the numerical flow calculation for the bounded domain.

E. Electrorotatinal torque model for a bounded domain

Squires and Bazant [6] and Saintillan et al. [15] computed two contributions to the angular velocity: one is due to the electrokinetic flow (ICEP torque) and the other is due to the electrorotational torque [dielectrophoretic (DEP) torque]. Thus, to complete our analysis, we need to consider the DEP torque due to the parallel electric field around a cylindrical metal, i.e., in thin-double-layer approximation, the Maxwell stress tensor just outside the double layer leads to an element

of torque equal to $d\mathbf{T}^{\text{DEP}}=\mathbf{x}\times(-\tfrac{1}{2}\varepsilon E_s^2)\mathbf{n}dl$, where E_s is purely tangential to surface S_p^+. In general, the DEP torque

$$\mathbf{T}^{\text{DEP}} = \int \mathbf{x}\times\left(-\frac{1}{2}\varepsilon E_s^2\right)\mathbf{n}dl \quad (11)$$

on S_p^+ is different from zero. That is, the external torque in Eq. (3) is different from zero and it is equal to the DEP torque. Note that, for a bounded problem, we refer the method that considers both the DEP and ICEP torques (i.e., $\mathbf{T}_t^{\text{ext}}=\mathbf{T}^{\text{DEP}}$) as method D, while we refer the method that considers just the ICEP torque (i.e., $\mathbf{T}_t^{\text{ext}}=0$) as method C.

F. Electrorotational torque model for an unbounded domain

By using Eq. (A3) in Appendix A and Eq. (11), we find that the electrorotational torque of the elliptical cylinder in an unbounded domain is

$$\mathbf{T}_t^{\text{DEP,unbounded}} = \frac{\pi}{2}\varepsilon c^2 E_0^2(\alpha^2-1)\sin 2(\theta+\psi)e_3. \quad (12)$$

Note that Eq. (12) is the same as the result provided in the classical book of Smythe [17] with zero relative dielectric constant, which gives electric field lines purely tangential to surface S_p^+. Since $\mathbf{\Omega}=\mathbf{T}/2\pi(b^2+c^2)\mu$ for the elliptical cylinder in the Stokes flow [16], the angular velocity due to the DEP is

$$\mathbf{\Omega}^{\text{DEP,unbounded}} = \frac{1}{4}\frac{\varepsilon E_0^2}{\mu}\frac{\alpha^2-1}{\alpha^2+1}\sin 2(\theta+\psi)e_3. \quad (13)$$

Thus, from Eqs. (10) and (13), we can estimate that the total angular velocity is

$$\Omega_t^{\text{unbounded}} = \frac{5}{4}\frac{\varepsilon E_0^2}{\mu}\frac{\alpha^2-1}{\alpha^2+1}\sin 2(\theta+\psi)e_3. \quad (14)$$

G. Simple model for a multi-rotary-ICEP valve

Fundamental requirements for the design of a rotary-ICEP valve are to achieve a maximum average flow velocity for an open state and to close at a minimum leak with a maximum angular velocity. Here, we consider a simple model for the design of a multi- (Nth) rotary-ICEP valve that has N elliptical cylinders with half lengths $b=w/2N$ as shown in Fig. 2(a). The Nth rotary valve has $N-1$ channels with a width $2b$ and two channels with a width b for an open state at the thin body limit of elliptical cylinders as shown in Fig. 2(b). By considering 2D Poiseuille flow, we can estimate that the flow amounts of the divided channels with a width $2b$ and b are $\frac{2}{3\mu}(\frac{\Delta P}{L})b^3$ and $\frac{2}{3\mu}(\frac{\Delta P}{L})(\frac{b}{2})^3$, respectively. Therefore, the total flow amount of the Nth rotary valve is $Q^{(N)}=2\frac{2}{3\mu}(\frac{\Delta P}{L})(\frac{b}{2})^3+(N-1)\frac{2}{3\mu}(\frac{\Delta P}{L})b^3=\frac{2}{3\mu}(\frac{\Delta P}{L})b^3(N-0.75)$. Thus, by considering $b=w/2N$, we can estimate a maximum average flow velocity $U_p(=Q^{(N)}/w)$ of the Nth rotary-ICEP valve in an open state as follows:
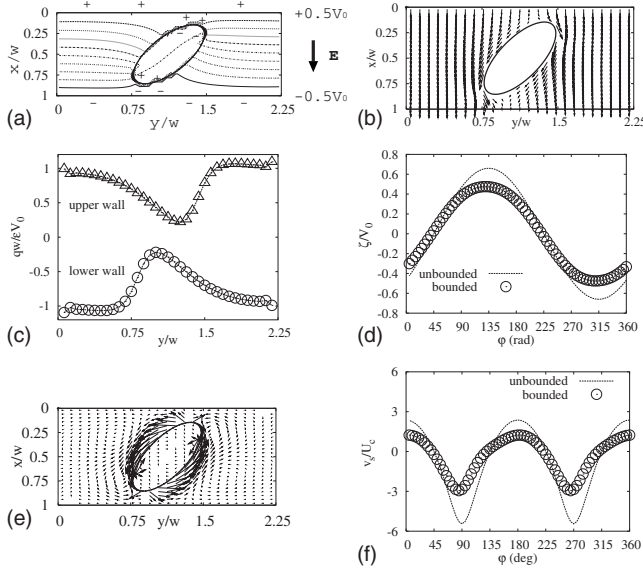
FIG. 3. Boundary effects. (a) Potential field, (b) electric field, (c) surface charge, (d) zeta potential, (e) flow field, and (f) slip velocity. Here, $c/w=0.2$, $\theta=3\pi/4$, $T_0\Delta P/\mu=0$, $\alpha(=b/c)=2.3$, and $T_0 U_c/w=0.01$, where T_0 is representative velocity. Throughout this paper, we use a set of typical values of $\mu=1.0$ mPa s, $w=100$ μm, and $T_0=1$ ms. Here, we obtain the values of $U_c=1.0$ mm/s, $\Delta P=0$ Pa, and $E_0=11.9$ kV/m.

$$U_p^{\text{open}} \simeq \frac{w^2}{12\mu} \frac{\Delta P}{L} \frac{N-0.75}{N^3}. \tag{15}$$

Further, an angular velocity of a rotary valve has a maximum value at $\theta=45°$ and $135°$ when $\psi=90°$ from Eq. (14). Note that $|\sin 2(\pi/4+\pi/2)|=|\sin 2(3\pi/4+\pi/2)|=1$. Therefore, from Eq. (14), we can estimate a maximum angular velocity of the Nth rotary-ICEP valve in a closing motion as follows:

$$\Omega^{\text{close}} \simeq \frac{5}{4} \frac{\varepsilon E_0^2}{\mu} \frac{\alpha^2-1}{\alpha^2+1}. \tag{16}$$

It should be noted that $\alpha(=b/c)=w/2Nc$ if c is constant for the Nth rotary valve. If the electrorotational torque is neglected intrinsically because of a bounded effect for the valve problems, we can obtain

$$\Omega^{\text{close}} \sim \frac{\varepsilon E_0^2}{\mu} \frac{\alpha^2-1}{\alpha^2+1}. \tag{17}$$

III. RESULTS

A. Boundary effects on ICEP

Figure 3 shows the boundary effects on electrophoresis when $\theta=135°$, $c/w=0.2$, and $\alpha(=b/c)=2.3$. Figures 3(a) and 3(b) show a potential and electric field in the rectangular channel, respectively. In Fig. 3(a), the symbols of "+" and "−" inside the domain stand for the induced charge and ion by the application of an electric field. In Fig. 3(b), an electric field around a metal cylinder is parallel to the surface on the metal because of the boundary condition. In this case, an
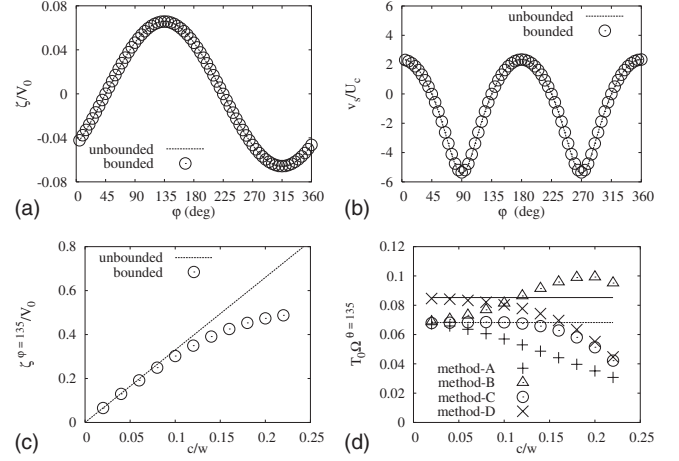

FIG. 4. Boundary effects on c/w. (a) Zeta potential ($c/w=0.02$), (b) slip velocity ($c/w=0.02$), (c) zeta potential vs c/w, and (d) angular velocity vs c/w. Here, $T_0\Delta P/\mu=0$, $\alpha(=b/c)=2.3$, and $T_0 U_c/w=0.01$; e.g., $\mu=1.0$ mPa s, $w=100$ μm, $T_0=1$ ms, $\Delta P=0$ Pa, $U_c=1.0$ mm/s, and $E_0=11.9$ kV/m. In (d), broken and solid lines show the analytical results by Eqs. (10) and (14), respectively (i.e., $\Omega^{\text{ICEP,unbounded}}$ and $\Omega_t^{\text{unbounded}}$, respectively).

elliptical metal cylinder is very close to both the upper and lower electrodes. Therefore, the boundary condition due to the existence of a thin double layer on the metal affects the surface charge distributions on the upper and lower walls as shown in Fig. 3(c). On the contrary, the charges of the surface on the upper and lower walls affect the zeta potential around a metal cylinder as shown in Fig. 3(d). Here, the maximum zeta potential of a bounded domain ($\zeta_{\max}^{\text{bounded}}/V_0=0.47$ at $\phi=135°$) is approximately 71% of that of an unbounded domain ($\zeta_{\max}^{\text{unbounded}}/V_0=0.66$ at $\phi=135°$). Further, Figs. 3(e) and 3(f) show the flow field and a slip velocity, respectively. As shown in Fig. 3(e), ions of the outer edge of the double layer slip along the tangential electric field and make a flow around a metal cylinder. Here, the maximum slip velocity of a bounded domain ($v_{s,\max}^{\text{bounded}}/U_c=1.2$ at $\phi=0°$) is approximately 50% of that of an unbounded domain ($\zeta_{\max}^{\text{unbounded}}/V_0=2.4$ at $\phi=0°$) as shown in Fig. 3(f). Thus, peak values of a zeta potential and a slip velocity around a metal are suppressed by the effects of electric field deformations when $2c\sim w$. Furthermore, although we use method D that considers both the ICEO and DEP flow in the calculation of Fig. 3(e), the flow field is almost the same as that by method C because of the suppression of electrorotational torque due to the bounded effect.

Figures 4(a) and 4(b) show the dependence of ζ and v_s on φ when $c/w=0.02$ and $\alpha(=b/c)=2.3$. As shown in Figs. 4(a) and 4(b), the values of a zeta potential and a slip velocity around a metal in a bounded domain agree well with those of an unbounded domain when $c/w=0.02$. It should be noted that this verifies that our numerical code is correct. Figures 4(c) and 4(d) show the dependence of ζ and Ω on c/w when $\alpha(=b/c)=2.3$. As shown in Figs. 4(c), as c/w decreases, ζ (at $\phi=135°$) of a bounded condition asymptotically approach the values predicted with the thin electric double-layer approximation in an unbounded domain [i.e., the values predicted by Eq. (8)]. Thus, the effects of the electric field de-
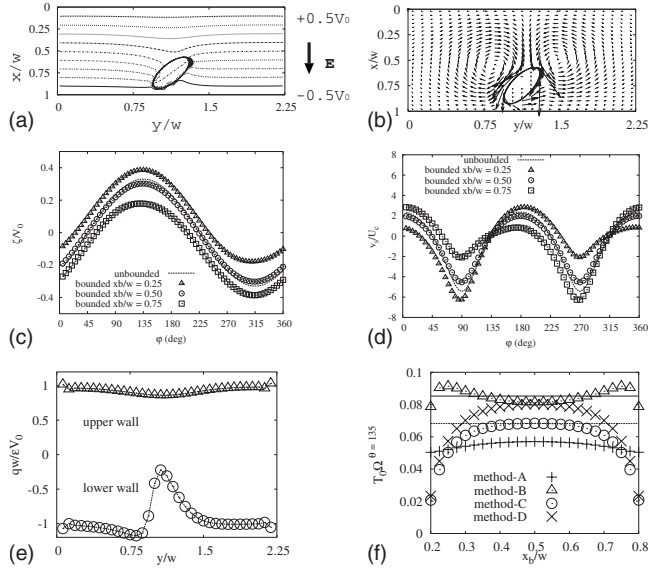
FIG. 5. Boundary effects on x_b/w. (a) Potential field ($c/w=0.1$, $x_b/w=0.75$), (b) flow field ($c/w=0.1$, $x_b/w=0.75$), (c) zeta potential [$c/w=0.1$, $\alpha(=b/c)=2.3$], (d) slip velocity [$c/w=0.1$, $\alpha(=b/c)=2.3$], (e) surface charge $c/w=0.2$, and (f) dependence of Ω on x_b. Here, $T_0\Delta P/\mu=0$, $\alpha(=b/c)=2.3$, and $T_0U_c/w=0.01$; e.g., $\mu=1.0$ mPa s, $w=100$ μm, $T_0=1$ ms, $\Delta P=0$ Pa, $U_c=1.0$ mm/s, and $E_0=11.9$ kV/m. In (f), broken and solid lines show the analytical results by Eqs. (10) and (14), respectively (i.e., $\Omega^{\text{ICEP,unbounded}}$ and $\Omega_t^{\text{unbounded}}$, respectively).

formations are negligible if $c \ll w$. Further, in Fig. 4(d), broken and solid lines show the analytical results of Eqs. (10) and (14), respectively (i.e., $\Omega^{\text{ICEP,unbounded}}$ and $\Omega_t^{\text{unbounded}}$, respectively), while plus (+), open triangle ($\triangle$), open circle ($\bigcirc$), and cross ($\times$) show the numerical results of methods A, B, C, and D, respectively. As shown in Fig. 4(d), the numerical results of methods C and D tend to the analytical results of Eq. (10) and (14), respectively, for c/w going to zero. Furthermore, from Fig. 4(d), we can find that in a perpendicular electric field, the boundary effect due to a fluid boundary condition accelerates the angular velocity of an elliptical metal cylinder, whereas the boundary effect due to an electric boundary condition decelerates the angular velocity of an elliptical metal cylinder. In particular, we can find that as c/w increases, the value of the DEP torque decreases and approaches zero.
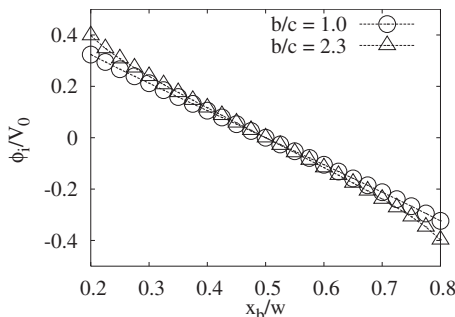

FIG. 6. Dependence of ϕ_i on x_b/w. Here, $c/w=0.1$ and $T_0U_c/w=0.01$; e.g., $w=100$ μm, $T_0=1$ ms, $U_c=1.0$ mm/s, and $E_0=11.9$ kV/m.
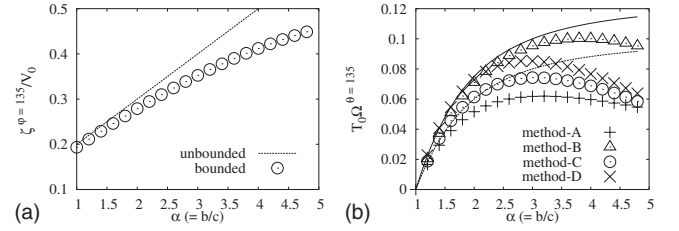

FIG. 7. Boundary effects on $\alpha(=b/c)$. Here, $\theta=3\pi/4$, $c/w=0.1$, $T_0\Delta P/\mu=0$, and $T_0U_c/w=0.01$; e.g., $\mu=1.0$ mPa s, $w=100$ μm, $T_0=1$ ms, $\Delta P=0$ Pa, $U_c=1.0$ mm/s, and $E_0=11.9$ kV/m. In (b), broken and solid lines show the analytical results by Eqs. (10) and (14), respectively (i.e., $\Omega^{\text{ICEP,unbounded}}$ and $\Omega_t^{\text{unbounded}}$, respectively).

Figure 5 shows the boundary effects on x_b/w when $\theta=135°$, $c/w=0.1$, and $\alpha(=b/c)=2.3$. Here, (x_b, y_b) is a position of the center of an elliptical metal cylinder. Figures 5(a) and 5(b) show potential and flow fields, respectively, for the metal positions $x/w=0.75$. In this case, we can find an asymmetrical zeta potential and slip velocity around a metal as shown in Figs. 5(c) and 5(d). This is the result from the redistribution of a surface charge on the lower electrode near the metal, i.e., when an elliptical metal cylinder approaches the lower wall as shown in Fig. 5(a), the negative surface charge on the lower electrode near the metal reduces considerably because of the repulsion due to the existence of the negative ions on the metal surface near the lower electrode as shown in Fig. 5(e). Figure 5(f) shows the dependence of Ω on x_b/w. Further, Fig. 6 shows the dependence of ϕ_i on x_b/w. It should be noted that the dependence of ϕ_i on x_b/w is slightly nonlinear and depended slightly on $\alpha(=b/c)$.

Figure 7 shows the dependence of ζ at $\phi=135°$ and Ω on $\alpha(=b/c)$ when $c/w=0.1$, $\theta=135°$, and $x_b/w=0.5$. As shown in Fig. 7(a), ζ^{bounded} asymptotically approaches $\zeta^{\text{unbounded}}$ as $\alpha(=b/c)$ decreases. In Fig. 7(b), the angular velocities of methods C and D asymptotically approach $\Omega^{\text{ICEP,unbounded}}$ and $\Omega_t^{\text{unbounded}}$, respectively.

B. Basic design of Nth rotary-ICEP valve

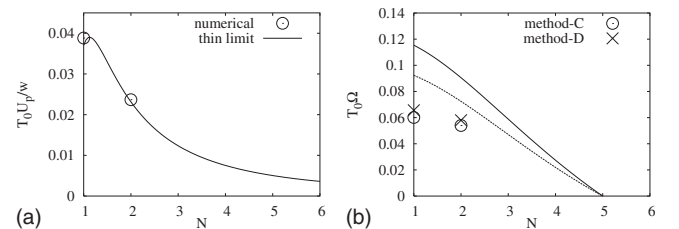Figure 8 shows the results of a basic design of a Nth

FIG. 8. Basic design of Nth rotary-ICEP valve. In (a), the symbol $\bigcirc$ shows the numerical results by the boundary element method, and the solid line shows the analytical results predicted by Eq. (15) (i.e., $U_p^{\text{open}}=(w^2/12\mu)(\Delta P/L)[(N-0.75)/N^3]$). In (b), open circle ($\bigcirc$) and cross ($\times$) show the numerical results by methods C and D, respectively, and solid and broken lines show the analytical results predicted by Eqs. (16) and (17), respectively (i.e., $\Omega^{\text{close}}\simeq(\varepsilon E_0^2/\mu)[1+(\alpha+1)^2/16\alpha][(\alpha^2-1)/(\alpha^2+1)]$ and $\Omega^{\text{close}}\simeq(\varepsilon E_0^2/\mu)[(\alpha^2-1)/(\alpha^2+1)]$). In here, $c/w=0.1$. Here, $L/w=2.25$, $T_0\Delta P/\mu=4$, and $T_0U_c/w=0.01$; e.g., $\mu=1.0$ mPa s, $w=100$ μm, $T_0=1$ ms, $\Delta P=4$ Pa, $U_c=1.0$ mm/s, and $E_0=11.9$ kV/m.
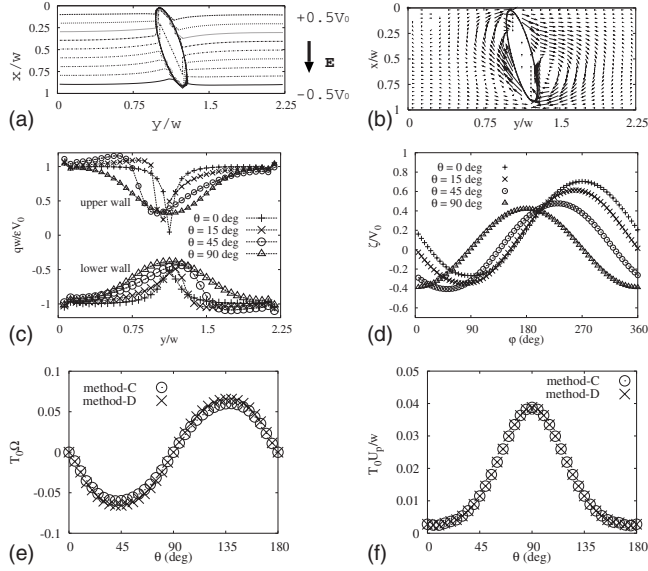
FIG. 9. Basic design of single rotary-ICEP valve. (a) Potential field ($\theta=15°$), (b) flow field ($\theta=15°$), (c) dependence of q on θ, (d) dependence of ζ on θ, (e) dependence of Ω on θ, and (f) dependence of U_p on θ. Here, the center of the single valve is anchored at $(x/w, y/w)=(0.47, 1.125)$; $\alpha(=b/c)=4.6$ and $c/w=0.1$. In (a)–(e), $T_0 \Delta P/\mu=0$ and $T_0 U_c/w=0.01$. In (f), $T_0 \Delta P/\mu=4$ and $T_0 U_c/w=0$; e.g., $T_0=1$ ms, $\mu=1$ mPa s, and $w=100$ μm.

FIG. 10. Basic design of twin rotary-ICEP valve. (a) Potential field ($\theta=15°$), (b) flow field ($\theta=15°$), (c) dependence of q on θ, (d) dependence of ζ on θ, (e) dependence of Ω on θ, and (f) dependence of U_p on θ. Here, the centers of the twin valve are anchored at $(x/w, y/w)=(0.25, 1.125)$ and $(0.75, 1.125)$, respectively; $\alpha(=b/c)=2.3$ and $c/w=0.1$. In (a)–(e), $T_0 \Delta P/\mu=0$ and $T_0 U_c/w=0.01$. In (f), $T_0 \Delta P/\mu=4$ and $T_0 U_c/w=0$; e.g., $T_0=1$ ms, $\mu=1$ mPa s, and $w=100$ μm.

rotary-ICEP valve by using Eqs. (15)–(17). Here, $w=100$ μm, $L/w=2.25$, $\Delta P=4$ Pa, $E_0=11.9$ kV/m, and $\mu=1$ mPa s. As shown in Fig. 8(a), the maximum U_p in an open state decreases rapidly as N increases. Further, as shown in Fig. 8(b), the maximum angular velocity in a closing motion Ω^{close} decreases as N increases if c/w is constant. Thus, selecting a small N number has advantages to obtain a large U_p in an open state and a large angular velocity in a closing motion. Therefore, as a realistic problem, considering a single or twin valve is enough to overview a design concept of a rotary-ICEP valve. Note that open circle and cross in Fig. 8 show the numerical results of methods C and D, respectively. In Fig. 8, the agreement of U_p between the numerical simulations and the thin limit is good, while the agreement of Ω is poor. This is because Eq. (16) just gives rough predictions based on the solution for an unbounded domain, while Eq. (15) gives good predictions based on the precise solution for 2D Poiseuille flows. In particular, the prediction of Eq. (16) that considers both the DEP and ICEP torques overestimates the angular velocity worse than that of Eq. (17) that just considers the ICEP torque, since the DEP torque is intrinsically small for the valve problem because of the bounded effect.

Figure 9 shows the results of a basic design of a single rotary-ICEP valve when $c/w=0.1$, $\alpha(=b/c)=4.6$, $x_b=0.47$, and $U_c=1$ mm/s. Figures 9(a) and 9(b) show the potential and flow fields of a single rotary-ICEP valve, respectively. Here, an elliptical metal cylinder is positioned off the center of the channel. Thus, the distribution of a surface charge is slightly asymmetrical between the upper and lower electrodes as shown in Fig. 9(c). Further, a zeta potential is biased to the positive direction as shown in Fig. 9(d). Here, if
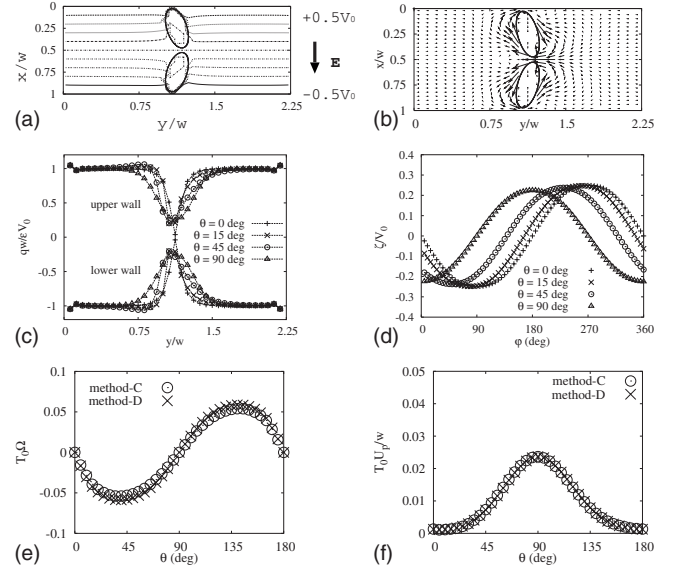
a metal cylinder locates at the center of the channel, a metal cylinder will not rotate from the closed state, and thus the single rotary-ICEP valve will not realize an open state in the presence of the pressure difference. It should be noted that the hydrodynamic force will always force the cylinder to be aligned with the flow field. However, because of a balance of clockwise and counterclockwise torques, the elliptical metal at $\theta=0°$ will not rotate in the 2D Poiseuille flow if we do not assume an artificial fluctuation. In Fig. 9(e), the maximum angular velocities of a bounded domain of methods C and D are 60 and 66 rad/s, which are 65% and 49% of those of an unbounded domain, respectively. Figure 9(f) shows the dependence of U_p on θ when $\Delta P=4$ Pa. In Fig. 9(f), the maximum and minimum velocities are 3.9 and 0.3 mm/s at $\theta=90°$ and $0°$, respectively.

Figure 10 shows the results of a basic design of a twin rotary-ICEP valve when $c/w=0.1$, $\alpha(=b/c)=2.3$, and $U_c=1$ mm/s. Figures 10(a) and 10(b) show the potential and flow fields of a twin rotary-ICEP valve, respectively. Here, we assume that $\theta^{\text{upper metal}}=-\theta^{\text{lower metal}}$, where $\theta^{\text{upper metal}}$ and $\theta^{\text{lower metal}}$ are θ of the upper and lower metal cylinders, respectively. Further, two elliptical metal cylinders are positioned at $x_b/w=0.25$ and 0.75. Thus, the distribution of a surface charge is symmetrical between the upper and lower electrodes as shown in Fig. 10(c). In Fig. 10(d), $\zeta/V_0=-0.249$ and $+0.249$ at $\phi=90°$ and $270°$, respectively, when $\theta=0°$, whereas $\zeta/V_0=-0.240$ and $+0.245$ at $\phi=90°$ and $270°$ when $\theta=15°$, respectively. Because of the symmetrical geometry where $\theta^{\text{upper metal}}=-\theta^{\text{lower metal}}$, the characteristics of the surface of one metal cylinder near the electrode and near the other metal cylinder are similar, but slightly different. In
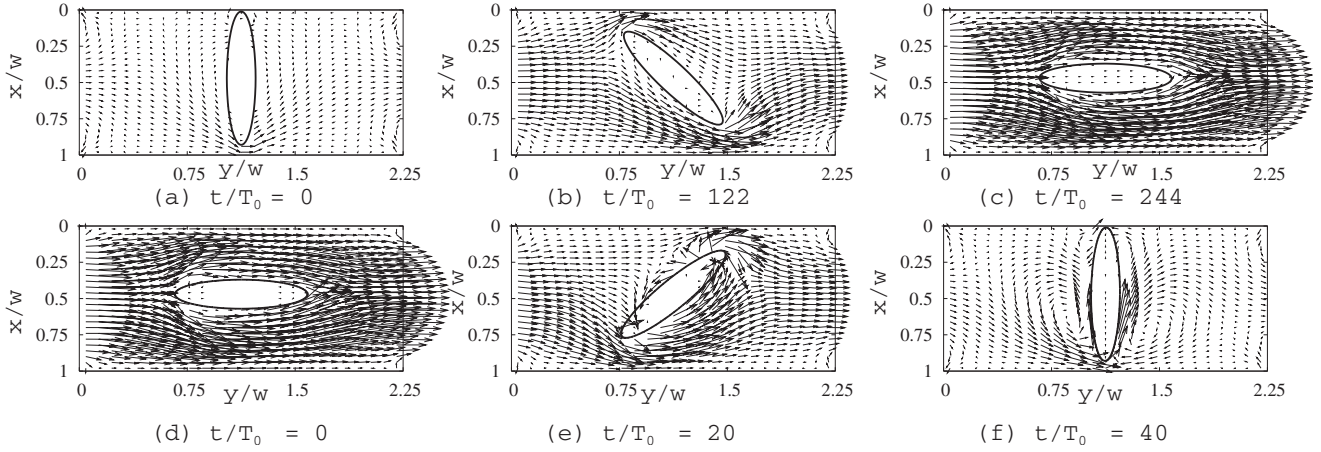
FIG. 11. Opening [(a)–(c) without an electric field] and closing [(d)–(f) with an electric field $(T_0 U_c / 0 = 0.01)$] motions and flow fields of single rotary-ICEP valve. Here, we use method D that considers both ICEO and DEP effects due to the parallel electric field on the metal cylinder, and the center of the single valve is anchored at $(x/w, y/w) = (0.47, 1.125)$; $T_0 \Delta P / \mu = 4$, $\alpha (=b/c) = 4.6$, and $c/w = 0.1$; e.g., $T_0 = 1$ ms, $\mu = 1$ mPa s, and $w = 100$ μm.

Fig. 10(e), the maximum angular velocities of a bounded domain of methods C and D are 54 and 58 rad/s, which are 75% and 61% of those of an unbounded domain [of Eqs. (10) and (14)], respectively. Figure 10(f) shows the dependence of U_p on θ when $\Delta P = 4$ Pa. In Fig. 10(f), the maximum and minimum velocities are 2.4 and 0.1 mm/s at $\theta = 90°$ and 0°, respectively.

C. Performance of single rotary-ICEP valve

Figure 11 shows the opening [Figs. 11(a)–11(c), without an electric field] and closing [Figs. 11(d)–11(f), with an electric field $E_0 = 11.9$ kV/m] motions and the flow fields for the single rotary-ICEP valve. As shown in Figs. 11(a)–11(c), an elliptical cylinder of the single valve continues to rotate counterclockwise by the presence of the pressure difference $\Delta P = 4$ Pa without an electric field because we place it slightly above the center line of the channel. As shown in

Figs. 11(d)–11(f), an elliptical cylinder of the single valve closes in a vertical electric field ($E_0 = 11.9$ kV/m). Although a single rotary valve that is placed on the center line of the channel (i.e., $x_b / w = 0.5$) has a problem that no torque due to an ICEP works if $\theta = 90°$ at $t = 0$ ms, we can avoid the problem by placing a valve slightly above the center line of the channel. Figure 12 shows the time evolution of a potential field [Figs. 12(a)–12(c)] and an electric field [Figs. 12(d)–12(f)] in a vertical electric field. Figure 13 shows the time evolution of a zeta potential [Figs. 13(a)–13(c)] and a slip velocity [Figs. 13(d)–13(f)] in a vertical electric field.

Figure 14 shows the performance of a single rotary-ICEP valve for an opening motion [Figs. 14(a)–14(c)] and a closing motion [Figs. 14(d)–14(f)] when $x_b / w = 0.47$, 0.48, and 0.49. Figures 14(a)–14(c) [Figs. 14(d)–14(f)] show the dependences of U_p, θ, and Ω on time t, respectively, in an opening motion [in a closing motion]. On one hand, for the conditions $x_b / w = 0.47$, 0.48, and 0.49, a single rotary valve
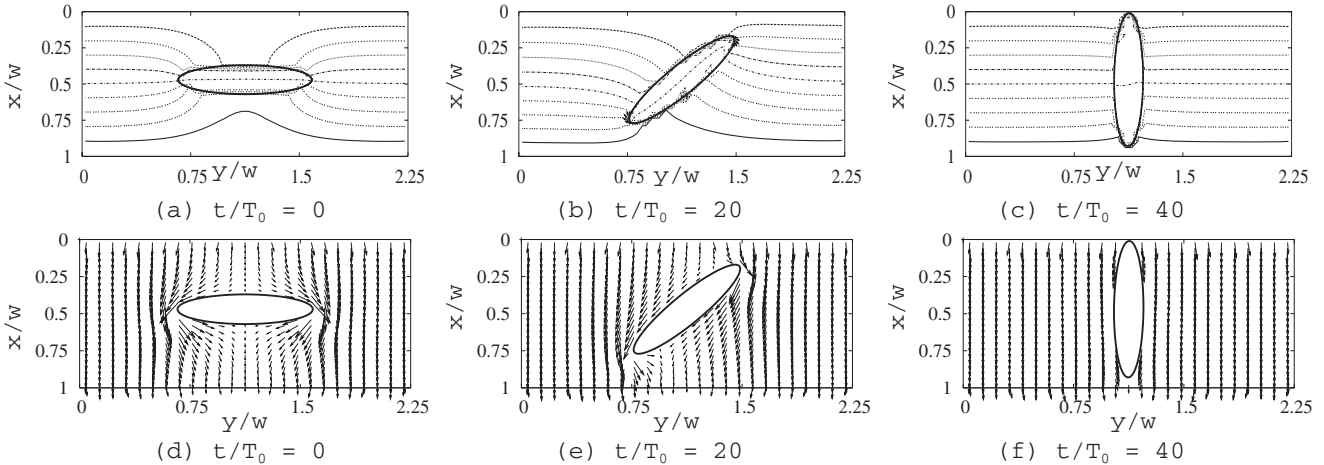

FIG. 12. Time evolution of [(a)–(c)] potential field and [(d)–(f)] electric field in a closing motion in a vertical electric field. Here, we use method D that considers both ICEO and DEP effects due to the parallel electric field on the metal cylinder, and the center of the single valve is anchored at $(x/w, y/w) = (0.47, 1.125)$; $T_0 \Delta P / \mu = 4$, $\alpha (=b/c) = 4.6$, $c/w = 0.1$, and $T_0 U_c / w = 0.01$; e.g., $T_0 = 1$ ms, $\mu = 1$ mPa s, $w = 100$ μm, $U_c = 1$ mm/s, and $E_0 = 11.9$ kV/m.
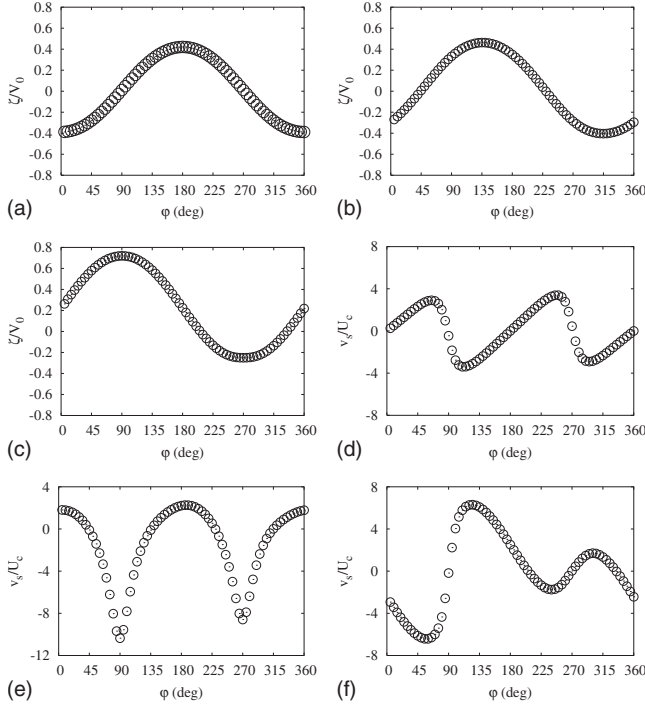
FIG. 13. Time evolution of [(a)–(c)] zeta potential and [(d)–(f)] slip velocity in a closing motion in a vertical electric field. In (a), (b), and (c) [(d), (e), and (f)], $t/T_0=0$, 20, and 40, respectively. Here, we use method D that considers both ICEO and DEP effects due to the parallel electric field on the metal cylinder, and the center of the single valve is anchored at $(x/w, y/w)=(0.47, 1.125)$; $T_0\Delta P/\mu=4$, $\alpha(=b/c)=4.6$, $c/w=0.1$, and $T_0U_c/w=0.01$; e.g., $T_0 = 1$ ms, $\mu=1$ mPa s, $w=100$ μm, $U_c=1$ mm/s, and $E_0 = 11.9$ kV/m.
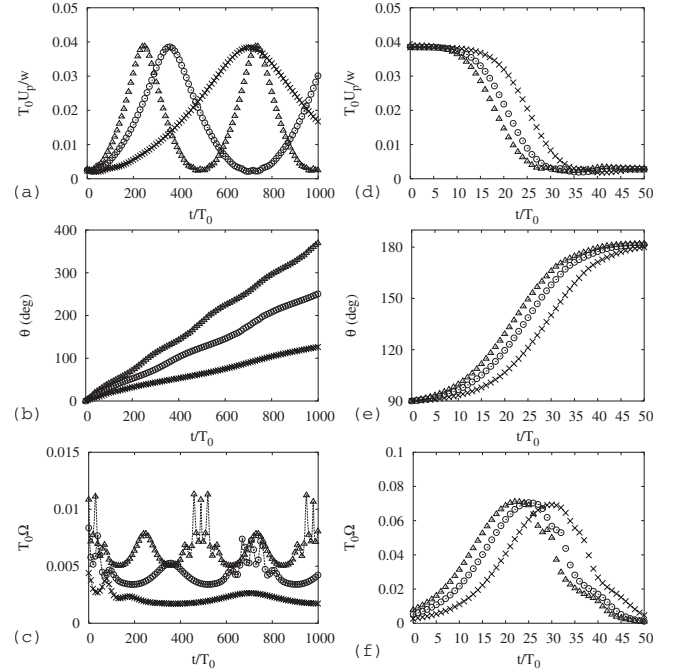

FIG. 14. Performance of single rotary-ICEP valve for an opening motion [(a)–(c) without an electric field] and a closing motion [(d)–(f) with an electric field $(T_0U_c/w=0.01)$]. Here, we use method D that considers both ICEO and DEP effects due to the parallel electric field on the metal cylinder, and open triangle, open circle, and cross show the numerical results for the single valve which center is anchored at $(x/w, y/w)=(0.49, 1.125)$, $(0.48, 1.125)$, and $(0.47, 1.125)$, respectively; $T_0\Delta P/\mu=4$, $\alpha(=b/c)=4.6$, and $c/w=0.1$.

in an opening motion has local maximum values of U_p =3.88, 3.86, and 3.84 mm/s at $t(=t_r^{\text{opening}})=244$, 359, and 699 ms, respectively, without an electric field as shown in Fig. 14(a). Here, t_r^{opening} is a response time in an opening motion, and the rotation of a single valve generates a pulsating flow with period $t_p^{\text{opening}}(=2t_r^{\text{opening}})$. On the other hand, for the conditions $x_b/w=0.47$, 0.48, and 0.49, a single rotary valve closes with $t(=t_r^{\text{closing}})=33$, 36, and 41 ms, respectively, by the application of a vertical electric field $E_0=11.9$ kV/m as shown in Fig. 14(d). Here, t_r^{closing} is a response time in a closing motion. Note that if we use method C instead of method D, $t(=t_r^{\text{closing}})=35$, 39, and 44 ms, respectively, i.e., if we neglect the DEP torque, we underestimate closing times about 10%. It should be noted that the angular velocities of the triangle symbols ($x_b=0.47$) in Fig. 14(c) spread wide around $t=0$, 500, and 1000 ms corresponding to $\theta=0°$, 180°, and 360° in Fig. 14(b) because there are various factors that increase and decrease the angular velocities in the small range near the angles due to the extremely small gap ($0.01w$) between the upper wall ($w=0$) and elliptical metal. That is we can expect a large counterclockwise torque at $\theta=0$ because we can neglect the flow through the small gap. However, by the small rotation of the elliptical metal, clockwise torque generates because of the flow between the upper wall and elliptical metal. Thus, the angular velocity decreases rapidly. Moreover, by the additional small rotation, we can ex-

pect another local maximum because of the increase in counterclockwise torque due to the flow distribution of 2D Poiseuille flow, and so on.

Figure 15 shows the dependence of U_p and t_r on x_b/w for a single rotary-ICEP valve. As shown in Fig. 15(a), both U_p^{max} and U_p^{min} are almost constant although they decrease gradually as x_b increases. As shown in Fig. 15(b), t_r^{opening} increases rapidly as x_b/w increases, whereas t_r^{closing} increases gradually from 33 to 41 ms. Thus, a single rotary-ICEP valve that is positioned off the center works well, i.e., it closes at high speed ($\sim$15 Hz) and can control the pulsating flow ($\sim$3.9 mm/s for open state).
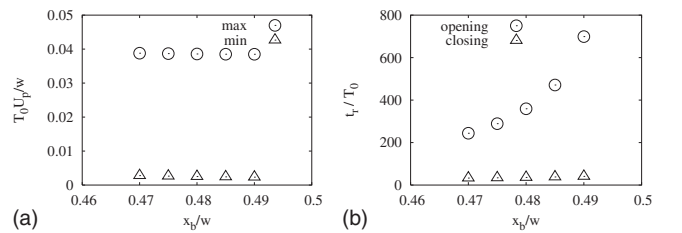

FIG. 15. Dependence of U_p and t_r on x_b/w for single rotary-ICEP valve. Here, we use method D that considers both ICEO and DEP effects due to the parallel electric field on the metal cylinder; $T_0\Delta P/\mu=4$, $\alpha(=b/c)=4.6$, and $c/w=0.1$; e.g., $T_0=1$ ms, $\mu =1$ mPa s, and $w=100$ μm.
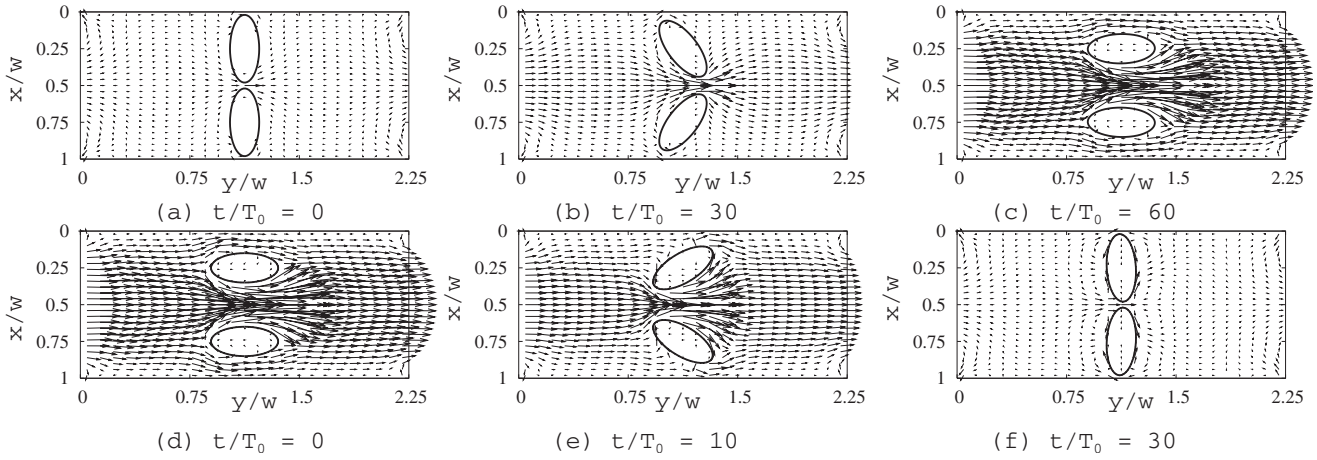
FIG. 16. Opening [(a)–(c) without an electric field] and closing [(d)–(f) with an electric field $E_0=11.9$ kV] motions of twin rotary-ICEP valve. Here, we use method D that considers both ICEO and DEP effects due to the parallel electric field on the metal cylinder, and the centers of the twin valve are anchored at $(x/w,y/w)=(0.25,1.125)$ and $(0.75,1.125)$, respectively; $T_0\Delta P/\mu=4$, $\alpha(=b/c)=2.3$, and $c/w=0.1$; e.g., $T_0=1$ ms, $\mu=1$ mPa s, and $w=100$ μm.

D. Performance of twin rotary-ICEP valve

Figure 16 shows the opening [Figs. 16(a)–16(c)] and closing [Figs. 16(d)–16(f)] motions and the flow fields for a twin rotary-ICEP valve. As shown in Figs. 16(a)–16(c) the upper and lower cylinders of the twin valve continue to rotate counterclockwise and clockwise, respectively, in an opening motion by the presence of the pressure difference $\Delta P=4$ Pa without an electric field because of the torque due to the Poiseuille flow. As shown in Figs. 16(d)–16(f), an elliptical cylinder of the twin valve closes in a vertical electric field ($E_0=11.9$ kV/m). Figure 17 shows the time evolution of a potential field [Figs. 17(a)–17(c)] and an electric field [Figs. 17(d)–17(f)] in a vertical electric field. Figure 18 shows the time evolution of a zeta potential [Figs. 18(a)–18(c)] and a slip velocity [Figs. 18(d)–18(f)] in a vertical electric field.

Figure 19 shows the performance of a twin rotary-ICEP valve for an opening motion [Figs. 19(a)–19(c)] and a clos-

ing motion [Figs. 19(d)–19(f)] when $\alpha(=b/c)=1.7$, 2.0, and 2.3. Figures 19(a)–19(c) [Figs. 19(d)–19(f)] show the dependences of U_p, θ, and Ω on time t, respectively, in an opening motion (in a closing motion). On one hand, a twin rotary valve in an opening motion has local maximum values of $U_p=2.83$, 2.61, and 2.42 mm/s at $t(=t_r^{opening})=24$, 34, and 60 ms, respectively, without an electric field as shown in Fig. 19(a). On the other hand, for the conditions $\alpha(=b/c)=2.0$ and 2.3, a twin rotary valve closes with $t(=t_r^{closing})=22$ and 21 ms, respectively, by the application of an electric field $E_0=11.9$ kV/m as shown in Fig. 19(d). Note that if we use method C, $t(=t_r^{closing})=23$ and 22 ms, respectively. It should be noted that the rotary-ICEP valve where $\alpha(=b/c)=1.7$ will not close by the application of an electric field $E_0=11.9$ kV/m because of the shortage of the torque due to an ICEP. Further, Figs. 20(a) and 20(b) show the time evolution of ϕ_i for the upper and lower metals, respectively, in a closing motion. As shown in Figs. 20(a) and 20(b), ϕ_i changes remarkably in the range $17<t<35$ ms when $\alpha(=b/c)=2.3$.
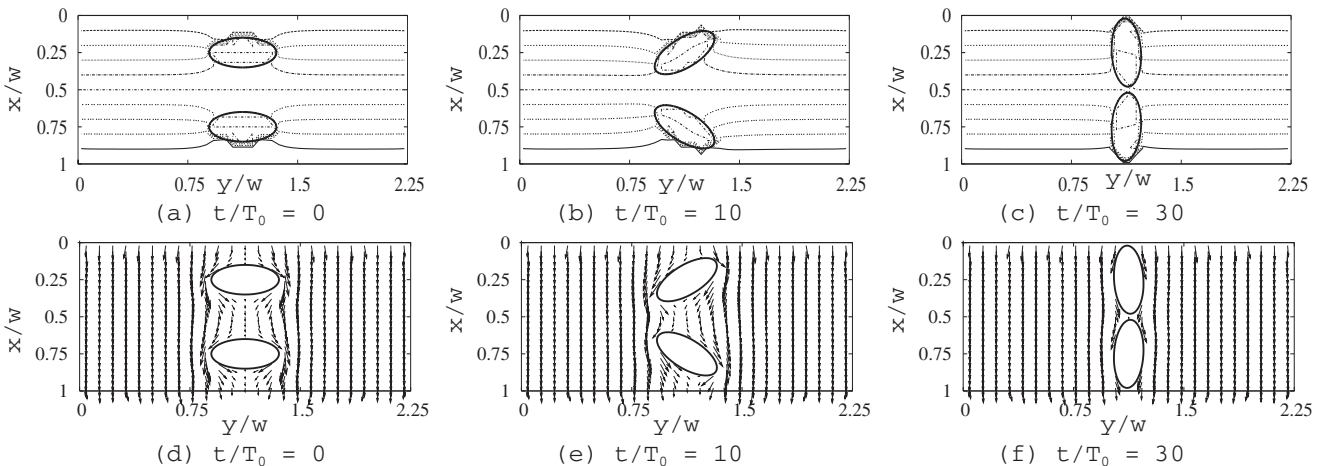

FIG. 17. Time evolution of potential and electric fields of twin rotary-ICEP valve by the application of a vertical electric field in an opening motion. Here, we use method D that considers both ICEO and DEP effects due to the parallel electric field on the metal cylinder, and the centers of the twin valve are anchored at $(x/w,y/w)=(0.25,1.125)$ and $(0.75,1.125)$, respectively; $T_0\Delta P/\mu=4$, $\alpha(=b/c)=2.3$, $c/w=0.1$, and $T_0U_0/w=0.01$; e.g., $T_0=1$ ms, $\mu=1$ mPa s, and $w=100$ μm.
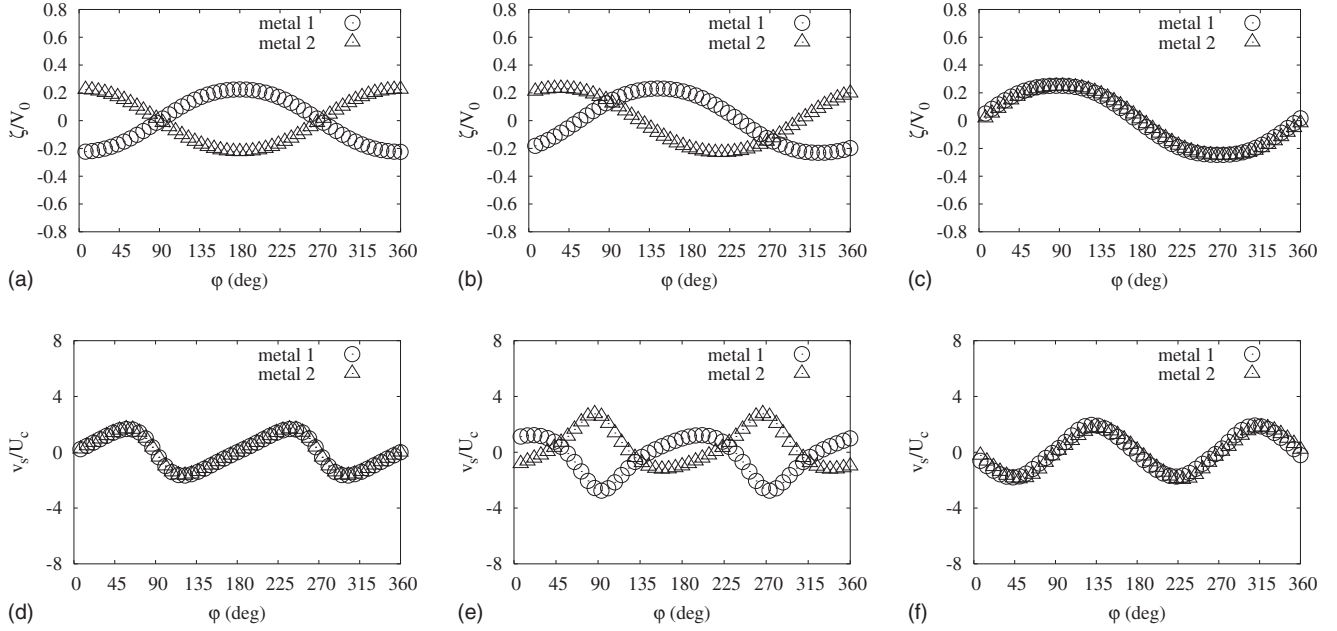
FIG. 18. Time evolution of a zeta potential and a slip velocity of twin rotary-ICEP valve by the application of a vertical electric field. In (a), (b), and (c) [(d), (e), and (f)], t/T_0=0, 20, and 40, respectively. Here, we use method D that considers both ICEO and DEP effects due to the parallel electric field on the metal cylinder, and the centers of the twin valve are anchored at $(x/w, y/w)=(0.25, 1.125)$ and $(0.75, 1.125)$, respectively; $T_0\Delta P/\mu=4$, $\alpha(=b/c)=2.3$, $c/w=0.1$, and $T_0U_c/w=0.01$; e.g., $T_0=1$ ms, $\mu=1$ mPa s, and $w=100$ μm.

Figure 21 shows the dependence of U_p and t_r on $\alpha(=b/c)$ for a twin rotary-ICEP valve. As shown in Fig. 21(a), both $U_p^{\max}$ and $U_p^{\min}$ decrease as $\alpha(=b/c)$ increases. As shown in Fig. 21(b), t_r^{opening} increase rapidly as b/c increases. It should be noted that the twin rotary-ICEP valve closes in the range $\alpha(=b/c)\gtrsim 2.0$. Thus, the twin rotary-ICEP valve closes at high frequency (~ 24 Hz) and a weak electric field (11.9 kV/m) in a microfluidic channel of 100 μm width and can control the pulsating pressure flow (~ 2.4 mm/s for open state).

E. Best rotary-ICEP valve

As a practical consideration, a valve often needs to work against external pressure gradient. Figure 22 shows the maximum pressure head our proposed valves can operate against. From Figs. 22(a) and 22(b), controllable maximum pressures for the single and twin rotary-ICEP valves of channel length L=2.25 μm are 32 and 8 Pa, respectively, i.e., controllable maximum pressure gradients of the single and twin rotary-ICEP valves are 142 and 36 kPa/cm, respectively. Note that we mainly use the condition that ΔP=4 Pa for L=2.25 μm ($\Delta P/L$=18 kPa/cm) throughout calculations except in Fig. 22, so that an average flow velocity for open state is approximately αU_c(=4.6 mm/s) that is a maximum flow value to be expected. Further, in Fig. 22, maximum and minimum average flow velocities for the single valve (at $T_0\Delta P/\mu$=4) are 3.9 and 0.19 mm/s, while those velocities for the twin valve are 2.2 and 0.26 mm/s, i.e., the values of $U_p^{\max}/U_p^{\min}$ for the single and twin rotary-ICEP valves are 20.1 and 8.4, respectively. Furthermore, a single rotary-ICEP valve is simpler than a twin rotary-ICEP valve. Therefore, from the viewpoint of practical applications, we believe that
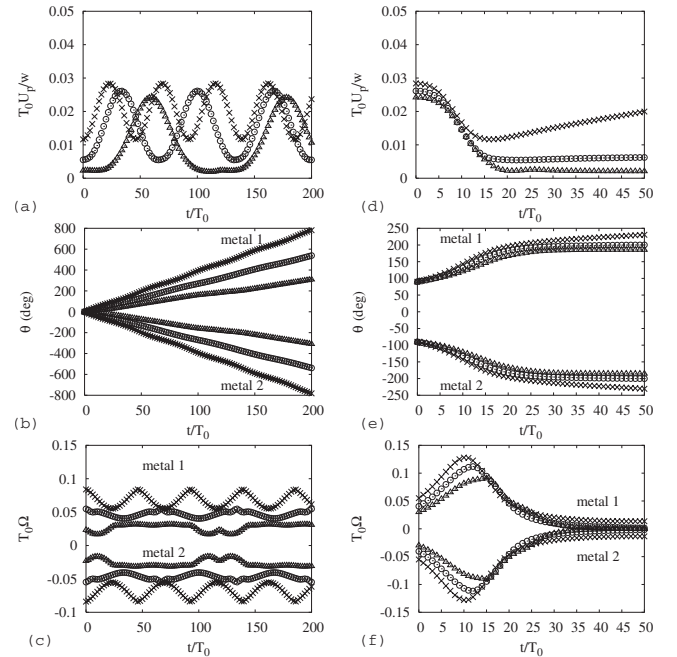

FIG. 19. Performance of twin rotary-ICEP valve for an opening motion [(a)–(c) without an electric field] and a closing motion [(d)–(f) with an electric field (T_0U_c/w=0.01)]. Here, we use method D that considers both ICEO and DEP effects due to the parallel electric field on the metal cylinder, and the centers of the twin valve are anchored at $(x/w, y/w)=(0.25, 1.125)$ and $(0.75, 1.125)$, respectively; $T_0\Delta P/\mu$=4, $\alpha(=b/c)$=2.3, and c/w=0.1; e.g., $T_0=1$ ms, $\mu=1$ mPa s, and $w=100$ μm. The symbols show the numerical results for a bounded domain, i.e., open triangle, open circle, and cross show the numerical results at b/c=2.3, 2.0, and 1.7, respectively.
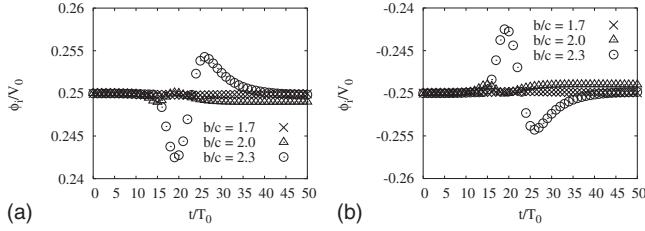
FIG. 20. ϕ_i vs t. (a) and (b) show the results of upper and lower mental, respectively, Here, the centers of the twin valve are anchored at $(x/w, y/w) = (0.25, 1.125)$ and $(0.75, 1.125)$, respectively; $T_0\Delta P/\mu = 4$, $c/w = 0.1$, and $T_0 U_c/w = 0.01$; e.g., $T_0 = 1$ ms, $\mu = 1$ mPa s, $w = 100$ μm, $U_c = 1$ mm/s, and $E_0 = 11.9$ kV/m.

a single rotary-ICEP valve is better than a twin rotary-ICEP valve and any other multi-rotary-ICEP valves, although the response frequency of a twin valve is larger than that of a single valve. Thus, we believe that a single rotary-ICEP valve is the best rotary-ICEP valve.

IV. DISCUSSION

Boundary effects on electrophoresis of colloidal cylinders have been analyzed by Keh *et al.* [18], and the effect of induced electro-osmosis on cylindrical particle next to a surface has been analyzed by Zhao and Bau [19]. However, the effect of ICEP on the rotation of an elliptical metal cylinder near a metal surface in a flow channel has been analyzed in this paper by the multiphysics coupled simulation technique between fluidics and electrostatics based on the boundary element method along with the thin-double-layer approximation. Based on the analysis of boundary effects on ICEP, we have extended ICEP to design a microfluidic system's component including a movable part, albeit the induced-charge electro-osmosis (ICEO) has been utilized to enhance mixing in principle [4,5,20], and it can also be exploited to pump the liquid [2,4–8,11–13,21,22]. Namely, we have shown that by the application of an electric field perpendicular to the flow channel, the elliptical metal cylinder in the channel rotates to be aligned with the electric field due to ICEP and the elliptical cylinder can block the flow, which serves as a valve. It should be noted that although the angular velocity of an elliptical metal due to ICEP is diminished by the electric
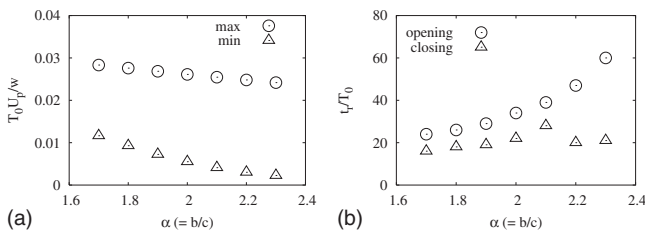

FIG. 21. Dependence of U_p and t_r on $\alpha(=b/c)$ for twin rotary-ICEP valve. Here, we use method D that considers both ICEO and DEP effects due to the parallel electric field on the metal cylinder, and the centers of the twin valve are anchored at $(x/w, y/w) = (0.25, 1.125)$ and $(0.75, 1.125)$, respectively; $T_0\Delta P/\mu = 4$, $T_0 U_c/w = 0.01$, and $c/w = 0.1$; e.g., $T_0 = 1$ ms, $\mu = 1$ mPa s, and $w = 100$ μm.
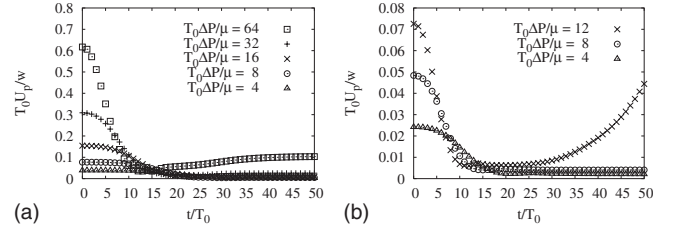

FIG. 22. Controllable maximum pressure. (a) The center of the single valve is anchored at $(x/w, y/w) = (0.48, 1.125)$. (b) The centers of the twin valve are anchored at $(x/w, y/w) = (0.25, 1.125)$ and $(0.75, 1.125)$, respectively. In (a) and (b), $T_0\Delta P/\mu = 4$, $T_0 U_c w = 0.01$, $L/w = 2.25$, and $c/w = 0.1$; e.g., $T_0 = 1$ ms, $\mu = 1$ mPa s, $w = 100$ μm, $\Delta P = 4$ Pa, $E_0 = 11.9$ kV/m, and $U_c = 1$ mm/s. Here, we use method D that considers both ICEO and DEP effects due to the parallel electric field on the metal cylinder,

boundary effects, it is accelerated by the fluidic boundary effects.

Further, from Eq. (17), we can estimate $\Omega^{\max} = \varepsilon E_0^2/\mu$ in the thin limit ($\alpha = b/c \rightarrow 0$) in water in an unbounded domain. Thus, if we consider a rotational electric field such as $\sin 2(\theta + \psi) = 1$, the response time is $t_r^{\min} = \pi\mu/2\varepsilon E_0^2$ and the response frequency is $f_r^{\max} = 1/2t_r^{\min}$, i.e., for $E_0 = 11.9$ kV/m, $t_r^{\min} = 16$ ms and $f_r^{\max} = 32$ Hz are ideal values. Therefore, the response frequencies of 15 and 24 Hz for the single and twin rotary-ICEP valves in a microfluidic channel are 44% and 69% of the ideal value (32 Hz).

We assume that boundary conditions at the two electrodes ($x=0$ and w) are those of fixed potential for the electrical problem and zero slip velocity for the mechanical problem. In order to have an electric field in the electrolyte, electrical current should go from one electrode to the other and, consequently, there must be Faradic reactions at the electrodes. This will surely generate problems such as bubble generation, changes in the electrolyte species, etc., although the problems are reduced to some extent by the application of ac electric fields. In addition, the electrodes might need to be ideally nonpolarizable in this context. In this case, one of the possibilities might be to have the electrodes further apart (to put the problems "the electrodes" outside the channel where the valve is) and to use porous walls, although we cannot deny that we still see that there could be fluid motion generated at the boundaries $x=0$ and w because of concentration polarization. In other words, if the channel walls are conducting so that electric field can be applied, the polarization of the electrolyte near the electrodes ($x=0, w$) will lead to shielding of the imposed dc electric field. In particular, a small voltage, such as 1.19 V ($=11.9$ kV/m $\times 100$ μm), might be particularly susceptible to polarization near the electrodes. Nevertheless, we believe that our predictions are still valid mainly because there are various ways for applying an electric field to the device, e.g., we can use the difference of charging time between electrodes and elliptical metals. Further, real electrodes are not ideally nonpolarizable and polarizable [23] and it is a realistic assumption that there is no tangential electric field that drives fluid as an ICEO flow at the boundaries $x=0$ and w. Furthermore, if the double layer is thin and Faradic reaction is fast, potential drop across the double layer will be uniform and the constant potential
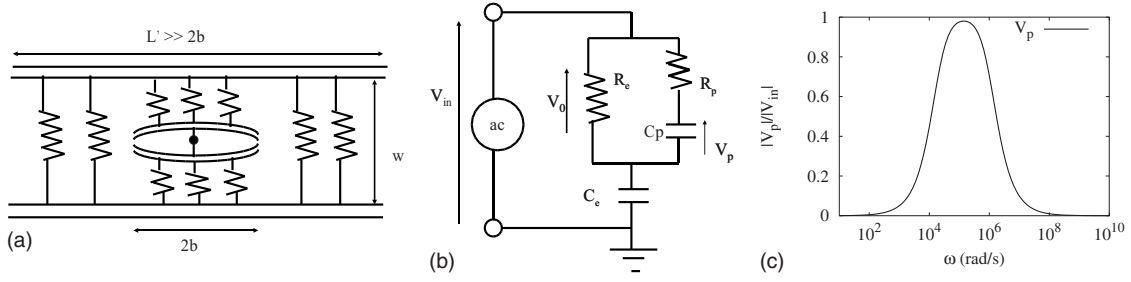
FIG. 23. ac analysis using a simple circuit model. (a) Schematic view of electro circuit model for ICEP value, (b) simple electro circut model, and (d) dependence of V_p on Ω for ICEP value.

boundary condition is still applicable, although the electrode will attract counterions and form electric double layer due to the electrostatics as long as there exists an electric potential on the electrode.

However, it is true that there are some difficulties if we consider dc electric fields. Thus, we need to consider ideally polarizable electrodes with ac electric fields, rather than ideally nonpolarizable electrodes with dc electric fields. Figure 23(a) shows the schematic view of the electric circuit model considered in this discussion. As shown in Fig. 23, ideally polarizable electrodes at $x=0$ and w are modeled [5,9,24] as the two capacitors of the capacitance $C_{e0}=\varepsilon L'd/\lambda_D$, where λ_D (~ 1 nm in water) is the Debye screening length, $L'(\gg 2b)$ is the length of electrodes, and d is a depth of the channel. Further, the polarizable elliptical metal is approximately modeled as the two capacitors of the capacitance $C_{p0}=\varepsilon 2bd/\lambda_D$. Furthermore, the resistance between electrodes is modeled as $R_e=w/\sigma_b L'd$, and the resistance between the electrode and elliptical metal is modeled as $R_p=\bar{w}/\sigma_b 2bd$, where $\sigma_b=\varepsilon D/\lambda_D^2$ is the bulk conductivity, $D(\sim 10^3 \ \mu\text{m}^2/\text{s})$ is an ion diffusivity, and $\bar{w}$ is the effective gap length between the electrode and elliptical metal. Since the gap length between the electrode and elliptical metal is $w-2c(80 \ \mu\text{m})$ and $w-2b(8 \ \mu\text{m})$ for $\psi=90°$ and $0°$, respectively, we can approximate $\bar{w}$ as $\bar{w}\simeq\sqrt{(w-2c)(w-2b)}$ $\sim 25 \ \mu\text{m}$ as a first attempt. Therefore, we can simplify the electrical circuit model as shown in Fig. 23(b). From the standard ac analysis, we obtain the complex internal voltage $\widetilde{V}_0(=V_0 e^{j\omega t})$ that is applied to the bulk region between two thin double layers of the electrodes as follows:

$$\widetilde{V}_0 = \frac{j\omega C_e R_e[j\omega C_p(R_e+R_p)+1]}{j\omega C_e R_e(j\omega C_p R_p+1)+[j\omega C_p(R_e+R_p)+1]}\widetilde{V}_{\text{in}},$$
(18)

where $\widetilde{V}_{\text{in}}$ is the complex external voltage that is applied between the electrodes including thin double layers and ω is a driving angular velocity of the ac external voltage. By considering $R_p\gg R_e$ (because of $L'\gg 2b$ and $w\sim\bar{w}$), we can approximate $\widetilde{V}_0$ as $\widetilde{V}_0\simeq[j\omega\tau_e/(j\omega\tau_e+1)]\widetilde{V}_{\text{in}}$, where $\tau_e=R_e C_e$ $=\lambda_D w/2D$ ($\simeq 1$ nm $\times 100 \ \mu\text{m}/2\times 10^{-9}$ m^2/s ~ 0.05 ms) is a charging time for the electrode. Thus,

$$|\widetilde{V}_0| \simeq \frac{\omega\tau_e}{\sqrt{(\omega\tau_e)^2+1}}|\widetilde{V}_{\text{in}}|.$$
(19)

Further, the complex voltage $\widetilde{V}_p$ across C_p is $\widetilde{V}_p=[1/(j\omega\tau_p+1)]\widetilde{V}_0\simeq[1/(j\omega\tau_p+1)][j\omega\tau_e/(j\omega\tau_e+1)]\widetilde{V}_{\text{in}}$, where τ_p

$=R_p C_p=\lambda_D\bar{w}/2D$ ($\simeq 1$ nm $\times 25 \ \mu\text{m}/2\times 10^{-9}$ m^2/s ~ 0.01 ms) is a charging time for the elliptical cylinder. Thus,

$$|\widetilde{V}_p| = \frac{1}{\sqrt{(\omega\tau_p)^2+1}}|\widetilde{V}_0| \simeq \frac{1}{\sqrt{(\omega\tau_p)^2+1}}\frac{\omega\tau_e}{\sqrt{(\omega\tau_e)^2+1}}|\widetilde{V}_{\text{in}}|.$$
(20)

Figure 23(c) shows the dependence of $\widetilde{V}_p$ on ω by using Eq. (20). From Fig. 23(c) or Eq. (20), our proposed device can work well around $\omega_0=(\tau_p^{-1}-\tau_e^{-1})/2\sim 0.4\times 10^5$ rad/s ($f_0=\omega_0/2\pi\sim 6$ kHz). Note that the ICEO flow around the elliptical cylinder is set into motion exponentially over the cylinder charging time τ_p, but is terminated exponentially over the longer electrode charging time τ_e as the bulk field is screened at the electrodes. In other words, electric fields persist in the bulk solution when the driving frequency is high enough ($\omega\tau_e>1$) that induced double layers do not have time to develop near the electrodes. Induced-charge electro-osmotic flows driven by applied ac fields can thus persist only in a certain band of driving frequencies, $\tau_e^{-1}<\omega<\tau_p^{-1}$. (Note that these kinds of arguments are seen in [5,9].)

By introducing dimensionless variables $\hat{\boldsymbol{v}}=\boldsymbol{v}/U_0$, $\hat{\boldsymbol{x}}=\boldsymbol{x}/L_0$, $\hat{\boldsymbol{t}}=\boldsymbol{t}/T_0$, and $\hat{p}=L_0 p/\mu U_0$, we can obtain the dimensionless form of Navier-Stokes equation [25], without an external force $\boldsymbol{g}$ as follows:

$$\beta\frac{\partial\hat{\boldsymbol{v}}}{\partial t} + \text{Re}\ \hat{\boldsymbol{v}}\cdot\hat{\boldsymbol{\nabla}}\hat{\boldsymbol{v}} = -\hat{\boldsymbol{\nabla}}\hat{p} + \hat{\nabla}^2\hat{\boldsymbol{u}},$$
(21)

where $\beta=\rho L_0^2/\mu T_0$ is unsteadiness parameter (the Stokes number), $\text{Re}=\rho U_0 L_0/\mu$ is the Reynolds number, and ρ is the density of the solution. Note that U_0, L_0, and T_0 are representative velocity, length, and time, respectively. The reciprocal number of frequency of rotation or equivalently the time of rotation is on the order of 10 ms. Thus, calculations may not be totally correct because of two quasistatic approximations: mechanical and electrical approximations. (a) The Reynolds and Stokes numbers associated with the angular frequency are not much smaller than ones under the condition that $w=100 \ \mu\text{m}$ and $E_0=11.9$ kV/m, i.e., $\text{Re}=\rho\Omega^{\text{max}}b^2/\mu \sim \rho\alpha U_c b/\mu \sim 1000$ kg/m$^3\times 5$ mm/s$\times 50$ $\mu\text{m}/1$ mPa s~ 0.25, and $\beta=\rho b^2/\mu T_0\sim 1000$ kg/m^3 $\times(50 \ \mu\text{m})^2/1$ mPa s~ 0.25. Therefore, under the condition that $w=100 \ \mu\text{m}$ and $E_0=11.9$ kV/m, the term $\beta\frac{\partial\hat{\boldsymbol{v}}}{\partial t}$ $+\text{Re}\ \hat{\boldsymbol{v}}\cdot\hat{\boldsymbol{\nabla}}\hat{\boldsymbol{v}}$ might be present in Eq. (21) to calculate more correctly, or we should reduce w; e.g., $\text{Re}\sim 0.0025$ and β

~ 0.0025 under the condition that $w = 10$ μm and $E_0 = 11.9$ kV/m. However, it is customary in microfluidic and colloidal systems to neglect the unsteady term $(\rho \, \partial \boldsymbol{v}/\partial t)$ in the Stokes equations, because ions diffuse more slowly than vorticity by a factor of $\rho D/\mu \simeq 10^{-3}$ [5]. Further, the condition that $w = 100$ μm and $E_0 = 11.9$ kV/m ($V_0 = 1.19$ V) is the most interesting condition for the wide range of biomedical applications. (b) The two typical times for charging a metal/electrolyte double layer are RC times, τ_p and τ_e. As mentioned before, these times are $\tau_p = \lambda_D \bar{w}/2D \sim 0.01$ ms and $\tau_e = \lambda_D w/2D \sim 0.05$ ms for water. Therefore, it seems that to use an electrical quasistatic approximation is justified for water. However, solutions that are used in biomedical applications have various values of λ_D in the range 1–100 nm. Thus, there is a possibility that to use an electrical quasistatic approximation may not be justified, e.g., if $\lambda_D = 100$ nm, $\tau_p \sim 1$ ms and $\tau_e \sim 5$ ms. In such a case, the electrical problem may need the following boundary condition at the surface of ellipsoid and electrodes: $\partial q/\partial t = j_n$, where $\partial q/\partial t$ is the derivative of surface charge in the double layer and j_n is the normal current arriving at them. Because of these two points, we may need to say that our calculations are a challenging approach to the problem.

V. CONCLUSION

In conclusion, we have proposed rotary-ICEP microvalves in water using hydrodynamic force due to induced-charge electrophoresis and numerically examined their performance. By the multiphysics coupled simulation technique between fluidics and electrostatics based on the boundary element method along with the thin-double-layer approximation, we find that (1) for the general problem an angular velocity of an elliptical metal cylinder is accelerated by the fluidic boundary effect and is decelerated by the electric boundary effect; (2) for the valve problem, the electric boundary effect is stronger than the fluidic boundary condition and thus it usually decelerates the angular velocity of the valve, because the elliptical metal cylinder is very close to the electrode; (3) to obtain a large average velocity in an opening state and a large angular velocity in a closing motion, single or twin rotary valves have more advantages than the multi- ($N \geq 3$) rotary-ICEP valves; (4) a single rotary-ICEP valve that is positioned off the center closes at high frequency (~ 15 Hz) and a weak electric field (11.9 kV/m) in a microfluidic channel and can control the pulsating pressure flow in an opening state; and (5) a twin rotary-ICEP valve closes at high frequency (~ 24 Hz) and a weak electric field (11.9 kV/m) in a microfluidic channel and can control the pulsating pressure flow in an opening state. We believe that actuators using ICEP will revolutionize the design concept of fluidic MEMS and can greatly contribute to many promising biomedical applications. In the future, we intend to evaluate other actuators using ICEP.

ACKNOWLEDGMENT

APPENDIX A: TANGENTIAL COMPONENT OF THE ELECTRIC FIELD

We used the solution for a 3D ellipsoid from [16] to obtain the 2D solution for an ellipse with a semimajor axis c and a semiminor axis b. On the surface S_p^+,

$$\phi = -\boldsymbol{x} \cdot \mathbf{G}_p^+ \cdot \boldsymbol{E}_\infty, \quad \boldsymbol{E}_p^+ = \mathbf{G}_p^+ \cdot \boldsymbol{E}_\infty, \tag{A1}$$

$$\mathbf{G}_p^+ = \left(1 + \frac{1}{\alpha}\right)\boldsymbol{e}_1 \otimes \boldsymbol{e}_1 + (1 + \alpha)\boldsymbol{e}_2 \otimes \boldsymbol{e}_2, \tag{A2}$$

where $\alpha = b/c$, $\boldsymbol{E}_p^+$ is the surface electric field, $\boldsymbol{x}$ is the position on the surface, and $\boldsymbol{e}_j$ is a unit coordinate vector. The symbol $\otimes$ is a tensor product, so that $(\boldsymbol{e}_j \otimes \boldsymbol{e}_j) \cdot \boldsymbol{E}_\infty = (\boldsymbol{e}_j \cdot \boldsymbol{E}_\infty)\boldsymbol{e}_j$. The tangential component of the electric field $\boldsymbol{E}_s$ is obtained thanks to

$$\boldsymbol{E}_s = (I - \boldsymbol{n}\boldsymbol{n}) \cdot \mathbf{G}_p^+ \cdot \boldsymbol{E}_\infty = (\boldsymbol{t} \cdot \boldsymbol{E}_p^+)\boldsymbol{t}, \tag{A3}$$

where $\boldsymbol{t}$ is the unit tangential vector to the surface.

Proof. For completeness, we provide a proof of this result. Using Eqs. (21) in [17], we have in two dimensions

$$\mathbf{G}_p^+ = \left[1 - \frac{bc}{2}W(b)\right]^{-1}\boldsymbol{e}_1 \otimes \boldsymbol{e}_1 + \left[1 - \frac{bc}{2}W(c)\right]^{-1}\boldsymbol{e}_2 \otimes \boldsymbol{e}_2,$$

$$W(u) = \int_0^\infty \frac{1}{(u^2 + \lambda)\sqrt{(b^2 + \lambda)(c^2 + \lambda)}}d\lambda.$$

These integrals can be computed analytically,

$$\frac{bc}{2}W(b) = \frac{bc}{2}\int_0^\infty \frac{d\lambda}{(b^2 + \lambda)^{3/2}(c^2 + \lambda)^{1/2}}$$

$$= bc\left[\frac{\sqrt{c^2 + \lambda}}{(b^2 - c^2)\sqrt{b^2 + \lambda}}\right]_0^\infty$$

$$= \frac{bc}{b^2 - c^2} - \frac{c^2}{b^2 - c^2} = \frac{1}{\alpha + 1}.$$

Similarly, $bcW(c)/2 = \alpha/(\alpha + 1)$. Thus,

$$\mathbf{G}_p^+ = \left(1 + \frac{1}{\alpha}\right)\boldsymbol{e}_1 \otimes \boldsymbol{e}_1 + (1 + \alpha)\boldsymbol{e}_2 \otimes \boldsymbol{e}_2.$$

APPENDIX B: 2D ANGULAR VELOCITY OF THE ELLIPTICAL CYLINDER IN AN UNBOUNDED DOMAIN

Proof. The translational and rotational parts of the motion can be treated separately. For the translational part, we write the velocity on the surface of the ellipse as $\boldsymbol{U}^{\text{unbounded}} + \boldsymbol{v}_s$. There should be no net force on the particle, so that

$$\int_{S_p^+}(\boldsymbol{n} \cdot \boldsymbol{x})(\boldsymbol{U}^{\text{unbounded}} + \boldsymbol{v}_s)dl = 0. \tag{B1}$$

The integral of $(\boldsymbol{n} \cdot \boldsymbol{x})$ can be computed easily using the Green's theorem and we find that

$$U^{\text{unbounded}} = -\frac{1}{2A_p} \int_{S_p^+} (\boldsymbol{n} \cdot \boldsymbol{x}) \boldsymbol{v}_s dl,$$

where $A_p = \pi bc$ is the area of the ellipse.

Similarly there should be no net torque on the particle, so that

$$\int_{S_p^+} (\boldsymbol{n} \cdot \boldsymbol{x})(|\boldsymbol{x}|^2 \boldsymbol{\Omega}^{\text{unbounded}} + \boldsymbol{x} \times \boldsymbol{v}_s) dl = 0. \qquad \text{(B2)}$$

From this equation, we obtain

$$\boldsymbol{\Omega}^{\text{unbounded}} = -\frac{1}{A_p(b^2 + c^2)} \int_{S_p^+} (\boldsymbol{n} \cdot \boldsymbol{x})(\boldsymbol{x} \times \boldsymbol{v}_s) dl.$$

We can now prove Eq. (10) using Eq. (7) for $\boldsymbol{v}_s$. Recall that $\boldsymbol{x}$ and $\boldsymbol{n}$ are equal to

$$\boldsymbol{x} = -c\alpha \sin \varphi \, \boldsymbol{e}_1 + c \cos \varphi \boldsymbol{e}_2,$$

$$\boldsymbol{n} = q_0^{-1}(-\sin \varphi \, \boldsymbol{e}_1 + \alpha \cos \varphi \boldsymbol{e}_2),$$

from which $\boldsymbol{n} \cdot \boldsymbol{x} = bq_0^{-1}$. The slip velocity $\boldsymbol{v}_s$ is given by Eq. (7). The length element can be shown to be equal to $dl = cq_0 d\varphi$.

Here, we can set $U^{\text{unbounded}} = \boldsymbol{0}$ because of the anchoring condition of our valves. However, we can show that $U^{\text{unbounded}} = \boldsymbol{0}$ even if we do not consider the anchoring condition. To show that $U^{\text{unbounded}} = \boldsymbol{0}$, we need to calculate the following integral:

$$\int_0^{2\pi} q_0^{-1} gt d\varphi,$$

where
$g = g(\varphi) = \frac{1}{2} \sin 2(\theta + \psi + \varphi) = \sin(\theta + \psi + \varphi) \cos(\theta + \psi + \varphi)$. However, we notice that $[q_0^{-1} g](\varphi + \pi) = [q_0^{-1} g](\varphi)$ while $\boldsymbol{t}(\varphi + \pi)$

$= -\boldsymbol{t}(\varphi)$. Therefore, this integral is equal to zero.

Moving on to $\boldsymbol{\Omega}^{\text{unbounded}}$, the cross product with x is equal to

$$\boldsymbol{x} \times \boldsymbol{v}^{(s)} = \frac{\varepsilon bc E_0^2 (1 + \alpha)^2 g}{\mu q_0^2} \boldsymbol{e}_3.$$

We therefore need to calculate the following integral:

$$\boldsymbol{\Omega}^{\text{unbounded}} = -\frac{\varepsilon E_0^2 b (1 + \alpha)^2}{\mu \pi c (1 + \alpha^2)} \left[\int_0^{2\pi} \frac{g}{q_0^2} d\varphi \right] \boldsymbol{e}_3.$$

The integral of g/q_0^2 can be computed analytically,

$$\frac{g}{q_0^2} = \frac{\sin(\theta + \psi + \varphi) \cos(\theta + \psi + \varphi)}{\alpha^2 \cos^2 \varphi + \sin^2 \varphi}.$$

If we expand $\sin(\theta + \psi + \varphi) \cos(\theta + \psi + \varphi)$, we obtain three terms, with $\cos^2 \varphi$, $\sin^2 \varphi$, and $\cos \varphi \sin \varphi$. Because of the antisymmetry $\cos(-\varphi) \sin(-\varphi) = -\cos \varphi \sin \varphi$, the last term makes no contribution. We are left with

$$\frac{\sin 2(\theta + \psi)}{2} \int_0^{2\pi} \frac{\cos^2 \varphi - \sin^2 \varphi}{\alpha^2 \cos^2 \varphi + \sin^2 \varphi} d\varphi$$

$$= \pi \sin 2(\theta + \psi) \frac{1 - \alpha}{\alpha(1 + \alpha)}.$$

Inserting this result for $\int g/q_0^2$ into the previous equation for $\boldsymbol{\Omega}^{\text{unbounded}}$, we finally obtain

$$\boldsymbol{\Omega}^{\text{unbounded}} = -\frac{\varepsilon E_0^2}{\mu} \frac{1 - \alpha^2}{1 + \alpha^2} \sin 2(\theta + \psi) \boldsymbol{e}_3.$$

[1] J. Melin and S. Quake, Annu. Rev. Biophys. Biomol. Struct. **36**, 213 (2007).

[2] S. Gangwal, O. J. Cayre, M. Z. Bazant, and O. D. Velev, Phys. Rev. Lett. **100**, 058302 (2008).

[3] K. A. Rose, J. A. Meier, G. M. Dougherty, and J. G. Santiago, Phys. Rev. E **75**, 011503 (2007).

[4] M. Z. T. Bazant and T. M. Squires, Phys. Rev. Lett. **92**, 066101 (2004).

[5] T. M. Squires and M. Z. T. Bazant, J. Fluid Mech. **509**, 217 (2004).

[6] T. M. Squires and M. Z. T. Bazant, J. Fluid Mech. **560**, 65 (2006).

[7] J. Urbanski, T. Thorsen, J. Levian, and M. Bazant, Appl. Phys. Lett. **89**, 143508 (2006).

[8] D. Burch and M. Z. Bazant, Phys. Rev. E **77**, 055303(R) (2008).

[9] M. Z. Bazant, K. Thornton, and A. Ajdari, Phys. Rev. E **70**, 021506 (2004).

[10] K. T. Chu and M. Z. Bazant, Phys. Rev. E **74**, 011501 (2006).

[11] B. D. Storey, L. R. Edwards, M. S. Kilic, and M. Z. Bazant, Phys. Rev. E **77**, 036317 (2008).

[12] A. Ramos, A. González, A. Castellanos, N. G. Green, and H. Morgan, Phys. Rev. E **67**, 056302 (2003).

[13] A. Ajdari, Phys. Rev. E **61**, R45 (2000).

[14] L. H. Olesen, H. Bruus, and A. Ajdari, Phys. Rev. E **73**, 056313 (2006).

[15] D. Saintillan, E. Darve, and S. Shaqfeh, J. Fluid Mech. **563**, 223 (2006).

[16] M. C. Fair and J. L. Anderson, J. Colloid Interface Sci. **127**, 388 (1989).

[17] W. R. Smythe, *Static and Dynamic Electricity* (McGraw-Hill Inc., New York, 1968), see Sec. 4.262.

[18] H. J. Keh, K. D. Horig, and J. Kuo, J. Fluid Mech. **231**, 211 (1991).

[19] H. Zhao and H. Bau, Langmuir **23**, 4053 (2007).

[20] H. Zhao and H. H. Bau, Phys. Rev. E **75**, 066217 (2007).

[21] A. González, A. Ramos, N. G. Green, A. Castellanos, and H. Morgan, Phys. Rev. E **61**, 4019 (2000).

[22] H. Sugioka, Phys. Rev. E **78**, 057301 (2008).

[23] J. Bockris, A. Reddy, and M. Gamboa-Aldecd, *Modern Electrochemistry 2A: Fundamentals of Electrics* (Springer, New York, 2001).

[24] A. Ramos, H. Morgan, N. Green, and A. Castellanos, J. Colloid Interface Sci. **217**, 420 (1999).

[25] C. Pozrikidis, *Introduction to Theoretical and Computational Fluid Dynamics* (Oxford University Press, Oxford, 1997).